Evolution of length scales and statistics of Richtmyer-Meshkov instability from direct numerical simulations

V. K. Tritschler,* M. Zubel, S. Hickel, and N. A. Adams
Institute of Aerodynamics and Fluid Mechanics, Technische Universität München, 85747 Garching, Germany
(Received 21 July 2014; published 1 December 2014)

In this study we present direct numerical simulation results of the Richtmyer-Meshkov instability (RMI) initiated by Ma = 1.05, Ma = 1.2, and Ma = 1.5 shock waves interacting with a perturbed planar interface between air and SF_6. At the lowest shock Mach number the fluids slowly mix due to viscous diffusion, whereas at the highest shock Mach number the mixing zone becomes turbulent. When a minimum critical Taylor microscale Reynolds number is exceeded, an inertial range spectrum emerges, providing further evidence of transition to turbulence. The scales of turbulent motion, i.e., the Kolmogorov length scale, the Taylor microscale, and the integral length, scale are presented. The separation of these scales is found to increase as the Reynolds number is increased. Turbulence statistics, i.e., the probability density functions of the velocity and its longitudinal and transverse derivatives, show a self-similar decay and thus that turbulence evolving from RMI is not fundamentally different from isotropic turbulence, though nominally being only isotropic and homogeneous in the transverse directions.

DOI: 10.1103/PhysRevE.90.063001 PACS number(s): 47.20.Ma, 47.27.ek, 47.40.Nm, 47.51.+a

I. INTRODUCTION

The Rayleigh-Taylor instability is an instability that occurs at the material interface between two fluids of different densities when one fluid is accelerated into the other one. In 1950, Taylor [1] provided a theoretical prediction of the growth rate of irregularities on the material interface between two fluids of different densities under constant acceleration. In his pioneering work Richtmyer [2] extended the theory of Taylor [1] to the impulsive acceleration of material interfaces. In the impulsive model of Richtmyer [2] the constant acceleration g of the material interface is replaced by an impulsive acceleration $\Delta u\delta(t)$. According to Richtmyer [2], the amplitude $a(t)$ of a single-mode perturbation with wave number k grows as

$$a(t) = (1 + k\Delta u A^+ t)a_0^+, \tag{1}$$

where $(\cdot)^+$ refers to values after the shock-interface interaction. a_0^+ is the postshock amplitude of the perturbed interface, $A^+ = (\rho_1 - \rho_2)/(\rho_1 + \rho_2)$ is the postshock Atwood number, and t is the time. Later, Richtmyer's theoretical predictions were experimentally verified by Meshkov [3], and the instability is thus known as the Richtmyer-Meshkov instability (RMI).

There are two hypotheses to explain the generation of vorticity at the material interface during shock-interface interaction [4]. The first one is based on baroclinic vorticity production; the other proposes that distorted transmitted and reflected waves create pressure variations across the material interface, which lead to tangential velocity perturbations. According to Brouillette [4] both hypotheses can be formally reconciled by noting that the induced tangential velocity components are responsible for the circulation. For more details see also Wouchuk and Nishihara [5], Wouchuk [6], and Zabusky [7]. The generated vorticity amplifies the initial interface perturbations, and if the initial energy input is sufficient, i.e., at sufficiently high Reynolds numbers, the flow evolves eventually into a turbulent mixing zone.

Because of the high Reynolds numbers and the associated small time and length scales, direct numerical simulations (DNSs) seemed to be unfeasible, and therefore large eddy simulations (LESs) have become the standard simulation approach to RMI [8–14]. Grinstein *et al.* [10] used a grid adaptive Eulerian code with implicit LES (ILES) modeling to study three-dimensional material mixing evolving from RMI. The ILES model combines a second-order Godunov-type scheme with the van Leer flux limiter. In the investigation of Schilling and Latini [11], the authors performed ILES with a high-order WENO scheme to study three-dimensional reshocked RMI to late times. In LES and ILES the energy-containing large scales are resolved and the dynamic interaction of unrepresented small scales with grid-resolved large scales is modeled by a subgrid-scale model. Due to the multiscale properties of RMI underresolved numerical simulations are very sensitive to the underlying numerical scheme, which does not only model the unresolved scales but also captures discontinuities such as shock waves and material interfaces; see Tritschler *et al.* [15].

Some recent investigations showed that the Kolmogorov length scale might be larger than assumed so far. In the experimental investigation of Weber *et al.* [16] the authors provided an estimate for the Kolmogorov length scale of a Ma = 1.5 shock accelerated shear layer. The estimate was obtained from fitting model spectra to the experimental spectra, which resulted in an estimate of 125 μm $\leqslant \eta \leqslant$ 214 μm. Tritschler *et al.* [17] found for the same shock Mach number a similar range for the Kolmogorov length scale 75 μm $\leqslant \eta \leqslant$ 224 μm. Consistent with these estimates Lombardini *et al.* [9] found $\eta \approx 620$ μm for RMI driven by a Ma = 1.05 shock wave and $\eta \approx 72$ μm for Ma = 5 long after the shock-interface interaction. Shortly after the shock-interface interaction the Kolmogorov scale can, however, be considerably smaller, being as small as $\eta \sim O(1)$ μm.

*volker.tritschler@aer.mw.tum.de

For the present investigation the shock tube size is scaled down in order to resolve all relevant length scales for Taylor microscale Reynolds numbers $\mathrm{Re}_\lambda \lesssim 140$. With this setup we are able to provide for the first time fully resolved results of the Richtmyer-Meshkov instability.

The paper is structured as follows: in Sec. II we outline the governing equations, which are solved with the numerical method given in Sec. III. The numerical setup is provided in Sec. IV. The results including grid convergence, the scales of turbulent motion, such as the integral length scale, Taylor microscale, and the Kolmogorov scale, as well as the probability density functions of the velocity and its longitudinal and transverse derivatives are presented in Sec. V. We conclude with a summary of our key findings in Sec. VI.

II. GOVERNING EQUATIONS

We solve the multicomponent Navier-Stokes equations in conservative form

$$\frac{\partial \boldsymbol{U}}{\partial t} + \nabla \cdot \boldsymbol{F}(\boldsymbol{U}) = \nabla \cdot \boldsymbol{F}_v(\boldsymbol{U}), \tag{2}$$

where $\boldsymbol{U}$ are the conserved variables:

$$\boldsymbol{U} = \left(\rho \;\; \rho\boldsymbol{u} \;\; E \;\; \rho Y_i\right). \tag{3}$$

The inviscid and viscous fluxes are given by

$$\boldsymbol{F}(\boldsymbol{U}) = \begin{pmatrix} \rho\boldsymbol{u} \\ \rho\boldsymbol{u}\boldsymbol{u} + p\underline{\boldsymbol{\delta}} \\ (E+p)\boldsymbol{u} \\ \rho\boldsymbol{u}Y_i \end{pmatrix}, \quad \boldsymbol{F}_v(\boldsymbol{U}) = \begin{pmatrix} 0 \\ \underline{\boldsymbol{\tau}} \\ \underline{\boldsymbol{\tau}} \cdot \boldsymbol{u} - \boldsymbol{q_c} - \boldsymbol{q_d} \\ -\boldsymbol{J_i} \end{pmatrix}. \tag{4}$$

Here we denote $\boldsymbol{u} = [u_1,u_2,u_3] = [u,v,w]$ as the velocity vector, p as the pressure, E as the total energy, ρ as the mixture density, and Y_i as the mass fraction of species i with $i = 1,2,\ldots,N$, where N is the total number of species. The identity matrix is $\underline{\boldsymbol{\delta}}$. The viscous stress tensor $\underline{\boldsymbol{\tau}}$ for a Newtonian fluid is

$$\underline{\boldsymbol{\tau}} = \overline{\mu}\,[2\underline{\boldsymbol{S}} - 2/3\underline{\boldsymbol{\delta}}\,(\nabla \cdot \boldsymbol{u})], \tag{5}$$

where $\overline{\mu}$ is the mixture viscosity and $\underline{\boldsymbol{S}}$ is the strain rate tensor. Equation (5) uses Stoke's hypothesis according to which the bulk viscosity is zero. We note that there is controversy in literature about the value of the bulk viscosity of large molecules, and setting it to zero may suppress some aspects of the real flow physics.

According to Fourier's law we define the heat conduction as

$$\boldsymbol{q_c} = -\overline{\kappa}\nabla T, \tag{6}$$

where $\overline{\kappa}$ is the mixture heat conductivity. The interspecies diffusional heat flux [18] is defined as

$$\boldsymbol{q_d} = \sum_{i=1}^{N} h_i \boldsymbol{J_i} \tag{7}$$

with

$$\boldsymbol{J_i} \approx -\rho\left(D_i \nabla Y_i - Y_i \sum_{j=1}^{N} D_j \nabla Y_j\right). \tag{8}$$

D_i indicates the effective binary diffusion coefficient of species i, and h_i is the individual species enthalpy. The equations are closed with the equation of state for an ideal gas

$$p(\rho e, Y_i) = (\overline{\gamma} - 1)\,\rho e, \tag{9}$$

where $\overline{\gamma}$ is the ratio of specific heat capacities of the mixture and e is the internal energy

$$\rho e = E - \frac{\rho}{2}\boldsymbol{u}^2. \tag{10}$$

The ratio of specific heat capacities of the mixture $\overline{\gamma}$ is calculated as

$$\overline{\gamma} = \frac{\overline{c_p}}{\overline{c_p} - \overline{R}}, \quad \text{with} \quad \overline{c_p} = \sum_{i}^{N} Y_i \frac{\gamma_i}{\gamma_i - 1}\overline{R}, \tag{11}$$

where $\overline{R}$ is the specific gas constant of the mixture with $\overline{R} = \mathcal{R}/\overline{M}$ and

$$\overline{M} = \left(\sum_{i}^{N} \frac{Y_i}{M_i}\right)^{-1}. \tag{12}$$

The viscosity and the thermal conductivity of the mixture, $\overline{\mu}$ and $\overline{\kappa}$, are calculated according to [19]

$$\overline{\mu} = \frac{\sum_{i=1}^{N} \mu_i Y_i / M_i^{1/2}}{\sum_{i=1}^{N} Y_i / M_i^{1/2}}, \qquad \overline{\kappa} = \frac{\sum_{i=1}^{N} \kappa_i Y_i / M_i^{1/2}}{\sum_{i=1}^{N} Y_i / M_i^{1/2}}. \tag{13}$$

The species specific viscosity μ_i is calculated from the Chapman-Enskog viscosity model

$$\mu_i = 2.6693 \times 10^{-6} \frac{\sqrt{M_i T}}{\Omega_{\mu,i}\sigma_i^2}, \tag{14}$$

where σ_i is the collision diameter and $\Omega_{\mu,i}$ is the collision integral [20] given as

$$\Omega_{\mu,i} = A(T_i^*)^B + C\exp\{DT_i^*\} + E\exp\{FT_i^*\}, \tag{15}$$

with $A = 1.16145$, $B = -0.14874$, $C = 0.52487$, $D = -0.7732$, $E = 2.16178$, and $F = -2.43787$, where the temperature is normalized by the Lennard-Jones energy parameter $T_i^* = T/(\epsilon/k)_i$.

The thermal conductivity is calculated from the species specific Prandtl number Pr_i as

$$\kappa_i = \frac{\gamma_i}{\gamma_i - 1} R_i \frac{\mu_i}{\mathrm{Pr}_i}, \tag{16}$$

and the mass diffusivities D_i are given by

$$D_i = \frac{\mu_i}{\rho \mathrm{Sc}_i}. \tag{17}$$

III. COMPUTATIONAL METHOD

Classical WENO approaches, albeit being formally high-order accurate, are too dissipative at discontinuities and in turbulent regions of the flow because in these regions the theoretical maximum order is never achieved. In order to reduce the excessive dissipation of classical WENO schemes Hu *et al.* [21] developed an adaptive central-upwind sixth-order accurate WENO scheme (WENO-CU6). This scheme significantly reduces the numerical dissipation, while preserving the shock-capturing properties of classical WENO schemes

and being only slightly computationally more complex than the standard fifth-order WENO scheme. Additionally, Hu and Adams [22] improved the scale separation of the original version, which makes the WENO-CU6 scheme also applicable to underresolved simulations.

In a recent investigation Hu *et al.* [23] introduced a dispersion-dissipation condition for finite-difference schemes. The dispersion-dissipation condition imposes a constraint on dissipation and dispersion errors in order to prevent backscatter of nonresolved spurious scales into the resolved-scale range. The modified version B according to Hu *et al.* [23] of the WENO-CU6 scheme is used in the present investigation.

Flux projection onto local characteristics is applied, which requires the Roe-averaged matrix to be calculated for the full multispecies system in Eq. (2) [24,25]. After reconstruction of the numerical fluxes at the cell boundaries the fluxes are projected back onto the physical field. A local switch to a Lax-Friedrichs flux is used as entropy fix; see, e.g., Toro [26]. Temporal integration is performed by a third-order total variation diminishing Runge-Kutta scheme [27].

The present numerical model has been tested and validated for shock induced turbulent multispecies mixing problems at finite Reynolds numbers [17,28,29]. Moreover, it has been demonstrated that it is a state-of-the-art approach to turbulent mixing processes evolving from RMI [15].

IV. NUMERICAL SETUP

The material interface separating air and SF_6 is accelerated by shock waves propagating with Ma = 1.05, Ma = 1.2, and Ma = 1.5. The corresponding postshock thermodynamic states are calculated from the Rankine-Hugoniot jump conditions with the preshock state defined by the stagnation condition $p_0 = 23\,000$ Pa and $T_0 = 298$ K. The Schmidt number of both gases is Sc = 1 and all other thermodynamic gas properties, which are taken from Poling *et al.* [19], are also constant; see Table I. The shock wave is initialized at $x = -L_x/4$ and propagates in the positive x direction. The transverse width L_{yz} of the shock tube is set to $L_{yz} = 0.01$ m, and periodic boundary conditions are used in the y and z direction. The fine-grid domain of the shock tube extends symmetrically in the positive and negative x direction about $x = 0$ m from $-L_x/2$ to $L_x/2$ with $L_x = 2L_{yz}$. A moving reference frame is applied such that the mixing zone remains within the fine-grid domain. The inflow and outflow boundary conditions are imposed very far from the fine-grid domain in order to avoid shock reflections. Outside of the fine-grid domain the computational grid is coarsened to reduce the computational costs. The fine-grid domain is discretized

TABLE I. Constant thermodynamic properties of air and SF_6.

Property	Air	SF_6
M_i [g mol^{-1}]	28.964	146.057
$(\epsilon/k)_i$ [K]	78.6	222.1
σ_i [Å]	3.711	5.128
γ_i	1.4	1.1
Pr_i	0.72	0.9

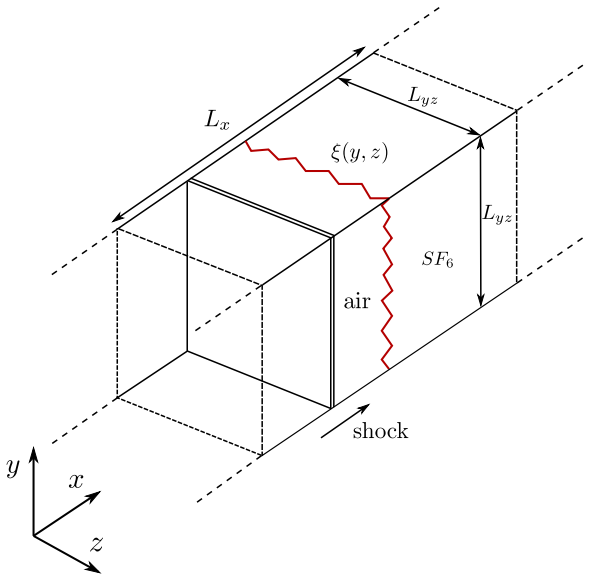

FIG. 1. (Color online) Schematic of the square shock tube showing the dimensions of the computational domain.

by three different grid resolutions $128^2 \times 256$, $256^2 \times 512$, and $512^2 \times 1024$ resulting in cubic cells of size $78\ \mu\mathrm{m} \gtrsim \Delta_{xyz} \gtrsim 19.5\ \mu\mathrm{m}$. The three grid resolutions are used for the convergence study, but only the results obtained on the finest grid are presented later. A schematic of the computational domain is given in Fig. 1.

In the present investigation the initial interface perturbation is given by

$$\xi(y,z) = a_1 \sin(k_0 y)\sin(k_0 z) + a_2 \sum_{n=1}^{13}\sum_{m=3}^{15} a_{n,m} \sin(k_n y + \phi_n)\sin(k_m z + \chi_m) \tag{18}$$

with the constant amplitudes $a_1 = -2.5 \times 10^{-4}$ m and $a_2 = 2.5 \times 10^{-5}$ m and wave numbers $k_0 = 10\pi/L_{yz}$, $k_n = 2\pi n/L_{yz}$, and $k_m = 2\pi m/L_{yz}$. The amplitudes $a_{n,m}$ and the phase shifts ϕ_n and χ_m are given by $a_{n,m} = \sin(nm)/2$, $\phi_n = \tan(n)$, and $\chi_m = \tan(m)$.

For the purpose of verifying grid convergence an initial length scale is imposed by a finite initial interface thickness

$$\psi(x,y,z) = \frac{1}{2}\left\{1 + \tanh\left[\frac{x - \xi(y,z)}{L_\rho}\right]\right\} \tag{19}$$

with $L_\rho = 0.001$ m being the characteristic initial thickness. The individual species mass fractions are imposed by $Y_{SF_6} = \psi$ and $Y_{\mathrm{air}} = 1 - \psi$. The time when the shock impacts the perturbed interface is $t = 0$ s.

V. RESULTS

A. Grid convergence

In order to verify the convergence, the average Kolmogorov length scale $\widetilde{\eta}$ within the inner mixing zone (imz) according to Tritschler *et al.* [15] as well as the compensated spectra of

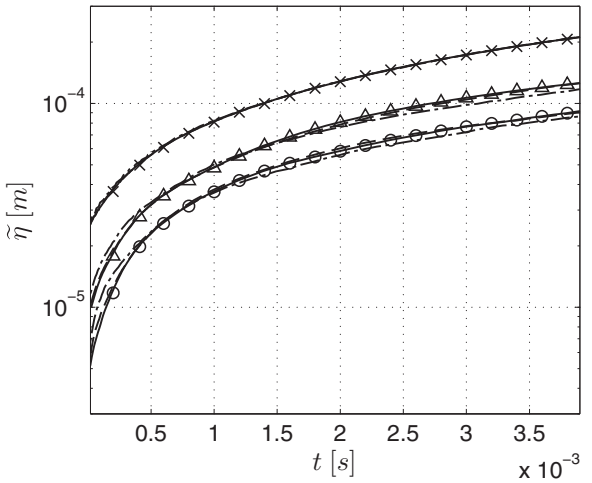

FIG. 2. Average Kolmogorov length scale of the inner mixing zone for Ma = 1.05 (crosses), Ma = 1.2 (triangles), and Ma = 1.5 (circles) computed on three different grid resolutions 128 (dashed-dotted), 256 (dashed), and 512 (solid lines with symbols).

enstrophy $E_\mathcal{E}$ are presented in Fig. 2 and Fig. 3 for the three grid resolutions.

We define the average Kolmogorov length scale as

$$\widetilde{\eta} = \left\langle \left(\frac{\langle \nu \rangle_{yz}^3}{\langle \varepsilon \rangle_{yz}} \right)^{1/4} \right\rangle_x , \tag{20}$$

where ε and ν are the viscous dissipation and the kinematic viscosity and $\langle \cdot \rangle$ denotes spatial averaging. The mean rate of viscous dissipation of kinetic energy is calculated from the single-point correlation of the fluctuating velocity gradients

$$\varepsilon = \nu \left[\frac{\partial u_i''}{\partial x_j} \frac{\partial u_i''}{\partial x_j} + \frac{\partial u_i''}{\partial x_j} \frac{\partial u_j''}{\partial x_i} - \frac{2}{3} \left(\frac{\partial u_i''}{\partial x_i} \right)^2 \right]. \tag{21}$$

For low-order statistics a resolution criterion of $k_{\max}\eta \geqslant 1$ is adequate for DNSs. For higher-order statistics, however, it was found (e.g., Ref. [30]) that a value of $k_{\max}\eta \geqslant 1.5$ is needed. Following this criterion, the finest grid resolution $\Delta_{xyz} \approx 19.5\ \mu$m sufficiently resolves turbulence with a minimal Kolmogorov length scale of $\eta_{min} \approx 9.3\ \mu$m. The average Kolmogorov length scale given in Fig. 2 verifies that for Ma = 1.05 and Ma = 1.2 the DNS resolution requirement is satisfied throughout the simulation on the finest grid resolution. For Ma = 1.5 it is satisfied after a short initial transient $t \gtrsim 130\ \mu$s.

The Kolmogorov length scale reaches a minimum right after the shock passage, which is $\widetilde{\eta} \approx 26\ \mu$m for Ma = 1.05 and decreases as the shock Mach number is increased to $\widetilde{\eta} \approx 5\ \mu$m for Ma = 1.5. After the shock passage the Kolmogorov length scale monotonically increases to $\widetilde{\eta} \approx 211\ \mu$m and $\widetilde{\eta} \approx 92\ \mu$m for Ma = 1.05 and Ma = 1.5, respectively, at the final time.

The compensated enstrophy spectra at $t = 50\ \mu$s, $t = 200\ \mu$s, $t = 500\ \mu$s, $t = 1000\ \mu$s, and $t = 3500\ \mu$s for Ma = 1.05, Ma = 1.2, and Ma = 1.5 are shown in Fig. 3. At Ma = 1.05 the peak enstrophy is fully resolved at all times and for all grid resolutions, whereas at Ma = 1.5 the peak enstrophy is not fully resolved at the earliest time $t = 50\ \mu$s. This is consistent with the average Kolmogorov length scale at these times. For the intermediate shock Mach number Ma = 1.2 the peak enstrophy is resolved on the two finest grids.

Note that enstrophy is a sensitive quantity and that other quantities converge already on coarser grids. From this, we conclude that our simulation results on the finest grid qualify as DNSs.

B. Scales of turbulent motion

The Taylor-microscale Reynolds number is defined as

$$\mathrm{Re}_\lambda = \frac{u''\lambda_T}{\nu}, \tag{22}$$

where u'' is the RMS velocity fluctuation obtained from Reynolds averaging, λ_T is the Taylor microscale, and ν is the kinematic viscosity. According to Dimotakis [31] the Taylor microscale Reynolds number must exceed $\mathrm{Re}_\lambda \geqslant 100$–$140$ or $\mathrm{Re} \geqslant 10^4$, if calculated as an outer-scale Reynolds number, in

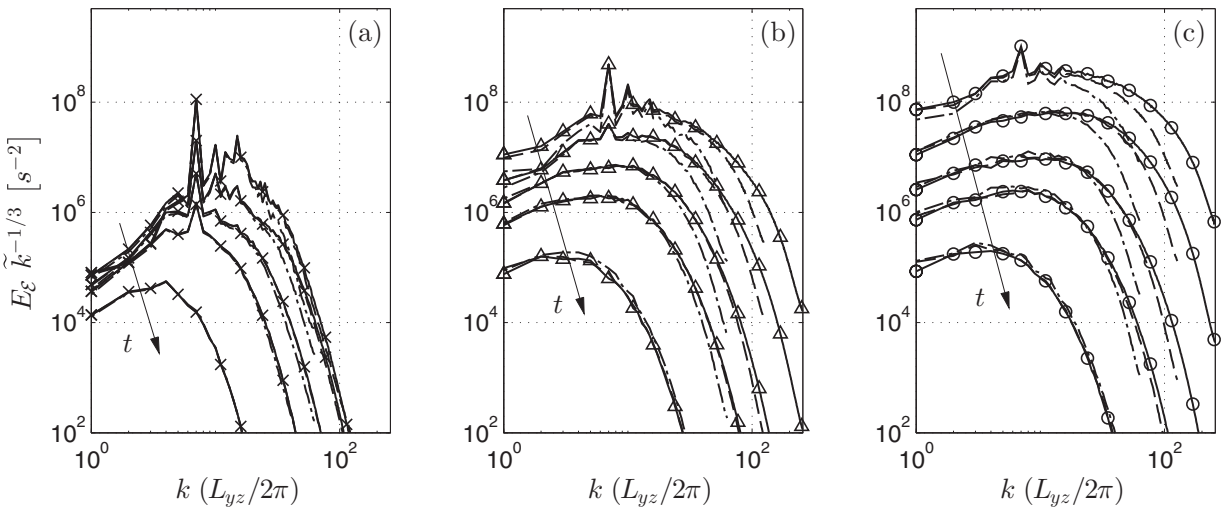

FIG. 3. Compensated enstrophy spectra for Ma = 1.05 (a), Ma = 1.2 (b), Ma = 1.5 (c) at $t = 50\ \mu$s, $t = 200\ \mu$s, $t = 500\ \mu$s, $t = 1000\ \mu$s, and $t = 3500\ \mu$s on three different grid resolutions 128 (dashed-dotted), 256 (dashed), and 512 (solid lines with symbols) with $\widetilde{k} = k\left(L_{yz}/2\pi\right)$.

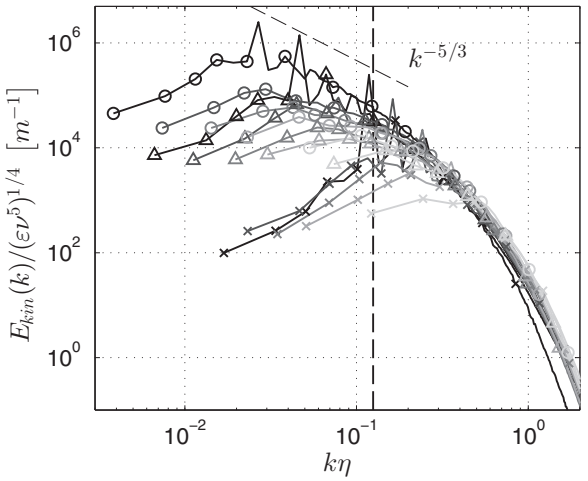

FIG. 4. Normalized turbulence kinetic energy spectra for Ma = 1.05 (crosses), Ma = 1.2 (triangles), and Ma = 1.5 (circles) at $t = 50$ μs, $t = 200$ μs, $t = 500$ μs, $t = 1000$ μs, and $t = 3500$ μs. The gray scale changes from black to light gray as time increases. The dashed vertical line at $k\eta = 1/8$ marks the beginning of the dissipation range.

order to observe fully developed turbulence. When the critical Reynolds number is exceeded a range of scales evolves that is independent from the large scales of motion and free from viscous effects. Only then does the inertial-range similarity concept of Kolmogorov [32] apply. The Taylor microscale Reynolds numbers depicted in Fig. 5 (a) show that for the two higher Mach numbers the Reynolds numbers are $\mathrm{Re}_\lambda \approx 143$ and $\mathrm{Re}_\lambda \approx 47$ after shock passage.

An inner viscous scale λ_ν [31], i.e., the upper limit of the dissipation range, can be estimated from the wave number k_ν where the spectrum begins to deviate from the inertial range spectrum, which is $k_\nu\eta \approx 1/8$ according to Dimotakis [31] who found this value by inspecting the data compilation of Saddoughi and Veeravalli [33]. The turbulence kinetic energy spectra normalized as proposed by Saddoughi and Veeravalli [33] are given in Fig. 4. The dashed line represents the inner viscous wave number according to $k_\nu\eta \approx 1/8$, which verifies that at this wave number all spectra begin to deviate from the inertial range scaling. Figure 4 also verifies that all spectra collapse within the dissipation range in agreement with Kolmogorov's theory.

From $k_\nu\eta \approx 1/8$ the inner viscous scale directly follows as

$$\lambda_\nu = \frac{2\pi}{k_\nu} \approx 50\eta. \tag{23}$$

The upper bound of the uncoupled range, the Liepmann-Taylor scale λ_L, is the smallest scale that can be directly generated from the outer scale δ. Based on experimental data Dimotakis [31] determined that the Liepmann-Taylor scale is proportional to the Taylor-microscale

$$\lambda_L \approx c_L\lambda_T, \tag{24}$$

with c_L as a flow-dependent parameter with a value of around $c_L \approx 5$; cf. Dimotakis [31], Zhou *et al.* [34], and Robey *et al.* [35].

The Taylor microscale λ_T is obtained from the curvature of the transverse spatial covariance of the velocity fluctuations $R_{t,i}(r,t)$ at $r = 0$:

$$\lambda_{T,i}(t) = \left[-\frac{1}{2}\frac{\partial^2 R_{t,i}(0,t)}{\partial r^2}\right]^{-1/2}, \tag{25}$$

with

$$R_{t,i}(r,t) = \frac{\langle u_i''(\vec{x},t)u_i''(\vec{x}+r\vec{e}_{j\neq i},t)\rangle}{\langle u_i''u_i''\rangle}, \quad \text{with} \quad i = 2,3. \tag{26}$$

The transverse covariance is evaluated in the homogeneous directions at each plane in the inner mixing zone with $-3 \leqslant r \leqslant 3$, giving $\lambda_{T,y}$ and $\lambda_{T,z}$. The directional Taylor microscales are averaged in the streamwise x direction, from which the effective mean Taylor microscale is calculated.

Dimotakis [31] argued that an uncoupled range of scales exists when $\lambda_L/\lambda_\nu \geqslant 1$. The uncoupled range is illustrated in Fig. 5(b) evolving between Liepmann-Taylor scale λ_L and the upper limit of the dissipation range λ_ν. In the present study only the highest Mach number case exceeds $\mathrm{Re}_\lambda > 100$ and should therefore exhibit a range of uncoupled scales. At Ma = 1.5 a range of uncoupled scales with $\lambda_L > \lambda_\nu$ evolves for $t \lesssim 400$ μs. At this time the Taylor microscale Reynolds number is $\mathrm{Re}_\lambda \approx 26$, which is smaller than the expected value of $\mathrm{Re}_\lambda > 100 - 140$ according to Dimotakis [31]; see Fig. 5(a). Because

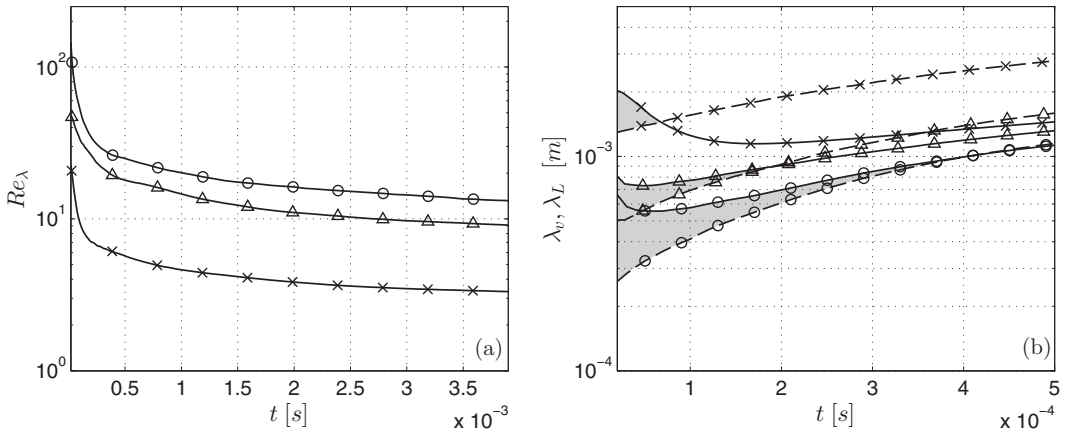

FIG. 5. Taylor microscale Reynolds number and uncoupled range of scales, given by the inner viscous scale λ_ν (dashed) and the Liepmann-Taylor scale λ_L (solid) for Ma = 1.05 (crosses), Ma = 1.2 (triangles), and Ma = 1.5 (circles).

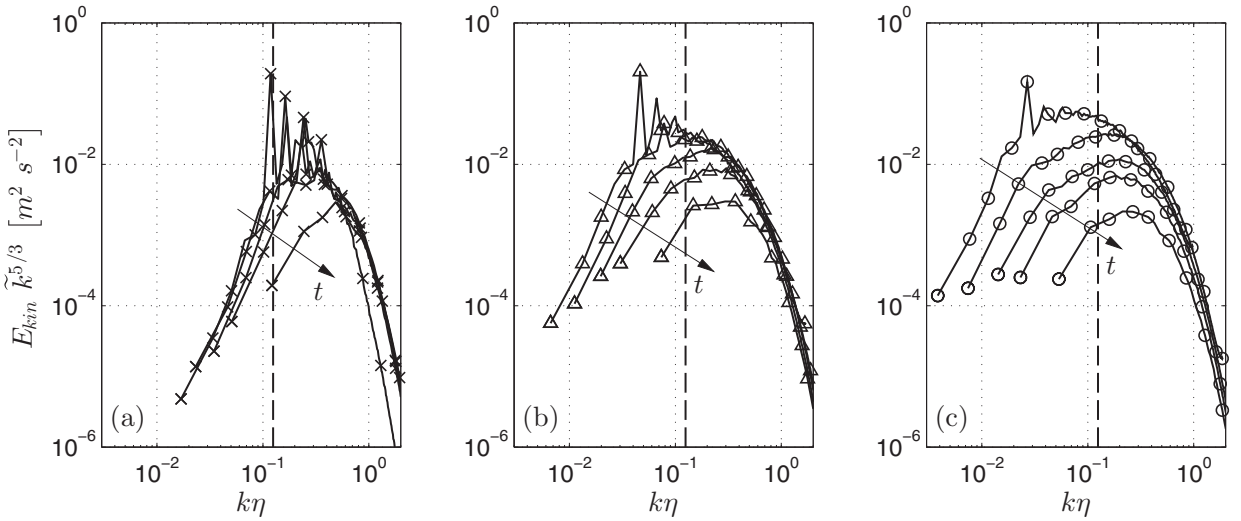

FIG. 6. Compensated spectra of turbulence kinetic energy for Ma = 1.05 (a), Ma = 1.2 (b), Ma = 1.5 (c) at $t = 50\ \mu$s, $t = 200\ \mu$s, $t = 500\ \mu$s, $t = 1000\ \mu$s, and $t = 3500\ \mu$s with $\widetilde{k} = k\eta$. The dashed vertical line at $k\eta = 1/8$ marks the beginning of the dissipation range.

of the uncertainties associated with the estimates for λ_L and λ_v and the shallow intersection of their curves a more realistic value for the critical Reynolds number in the present setup is $\mathrm{Re}_\lambda \gtrsim 35$–$80$.

Scales within the uncoupled range should exhibit a spectral scaling close to a $k^{-5/3}$ scaling. In Fig. 6 we show the compensated spectra of turbulence kinetic energy for all Mach numbers at 50 μs, 200 μs, 500 μs, 1000 μs, and 3500 μs over the Kolmogorov normalized wave number. The dashed line marks the beginning of the dissipation range at $k\eta = 1/8$. As observed in Fig. 5 the lowest Mach number case does not exhibit an uncoupled range of scales beyond $t \geqslant 60\ \mu$s. Accordingly, all scales are either affected by viscous effects or driven by the large-scale motion, such that no scales can become unstable and subsequently turbulent. As can be seen in Fig. 6(a) almost the full spectrum is within the dissipation range, which implies that the growth of the mixing zone is dominated by the large scales of motion and molecular diffusion.

For the medium Mach number, shown in Fig. 6(b), the energy-containing scales are also relatively close to the dissipation range with only a very narrow range of uncoupled scales immediately after the shock-interface interaction; see also Fig. 5(b). The existence of a $k^{-5/3}$ range is not evident, since the dominant wave numbers overlay an eventual inertial range at $t = 50\ \mu$s. At later times the spectrum becomes more shallow than Kolmogorov's scaling.

As the Mach number is increased to Ma = 1.5 an uncoupled range of scales develops during the first $t \approx 400\ \mu$s, which manifests in a narrow inertial range following approximately $k^{-5/3}$ at $t = 50\ \mu$s as can be seen in the compensated energy spectra in Fig. 6(c). At later times, however, an inertial range following $k^{-5/3}$ is not evident anymore. Only a very narrow band of uncoupled scales exists for $t \geqslant 200\ \mu$s, and thus, scales are likely to be either damped by viscous effects or affected by the large scales of motion beyond this time.

Scales within the uncoupled range can become unstable through nonlinear growth and mode coupling, which quickly removes the imprint of the initial perturbation. As seen in Fig. 6(a), if the energy-containing mode initially is in the dissipation range, the modes do not become unstable and are slowly dissipated. At the highest Mach number, Fig. 6(c), the modes become unstable, and the energy-containing mode quickly breaks down into smaller scales leaving no evidence of the initial perturbation.

Figure 7 shows the mixing zone width δ_x and the integral length scale Λ. The integral length scale is calculated from the longitudinal spatial velocity covariance [36]

$$\Lambda_i = \int_0^\infty R_{l,i}(r,t)\,dr, \tag{27}$$

with

$$R_{l,i}(r,t) = \frac{\langle u_i''(\vec{x},t)u_i''(\vec{x}+r\vec{e}_i,t)\rangle}{\langle u_i''u_i''\rangle}, \quad \text{with} \quad i = 2,3. \tag{28}$$

To compute the spatial velocity covariance in the whole domain $R_{l,i}(r,t)$ the Wiener-Khinchin theorem is applied. The theorem states that the autocorrelation function is the inverse Fourier

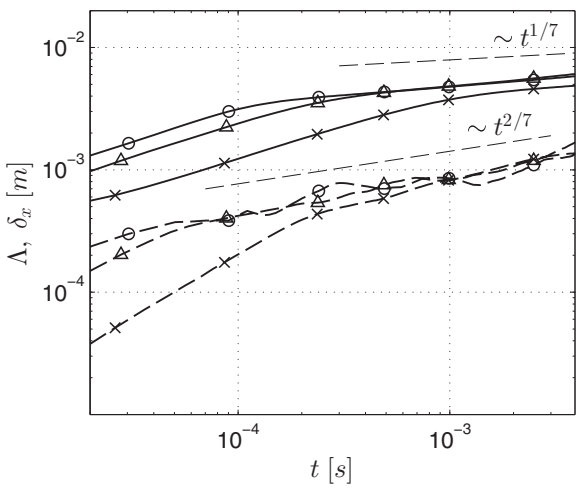

FIG. 7. The mixing zone width δ_x and the integral length scale Λ as a function of time.

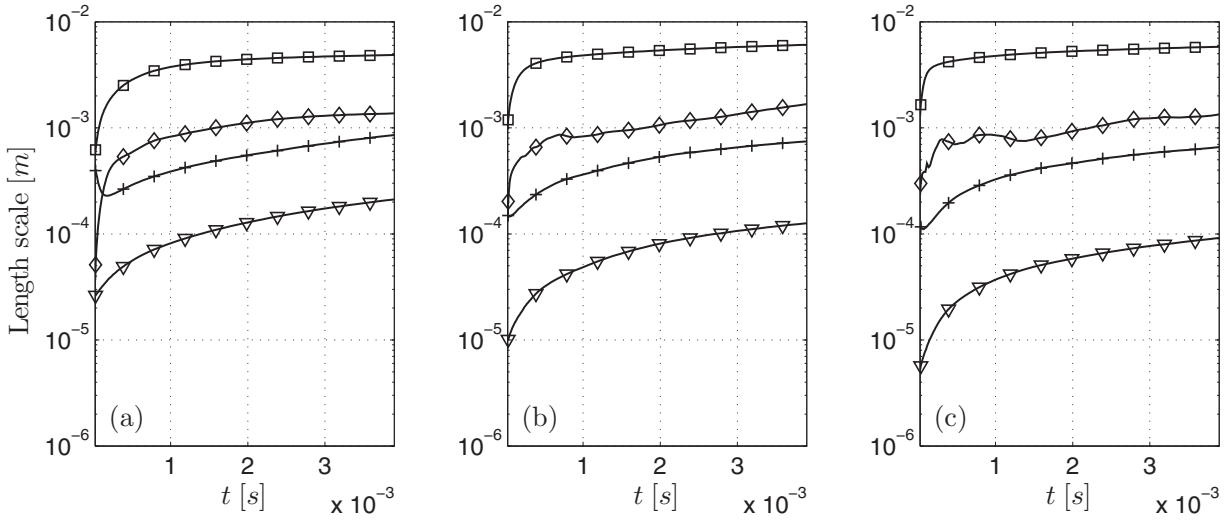

FIG. 8. Summary of length scales for Ma = 1.05 (a), Ma = 1.2 (b), and Ma = 1.5 (c). The solid lines with symbols represent the mixing zone width δ_x (squares), the integral length scale Λ (diamonds), the Taylor microscale λ_T (plus), and the Kolmogorov length scale η (triangles).

transform of its power spectrum

$$R_{l,i}(r,t) = \mathcal{F}^{-1}[\hat{u}_i''^{*}\hat{u}_i'']. \tag{29}$$

Integration of $R_{l,i}(r,t)$ leads to longitudinal integral scales in the y and z direction, Λ_y and Λ_z. The directional integral length scales Λ_i are averaged in the streamwise x direction from which the effective integral length scale Λ is calculated.

The mixing zone width is defined as

$$\delta_x(t) = \int_{-\infty}^{\infty} 4\langle Y_{SF_6}\rangle_{yz}(1 - \langle Y_{SF_6}\rangle_{yz})dx, \tag{30}$$

where $\langle\cdot\rangle_{yz}$ denotes ensemble averaging in the cross-stream yz plane.

The mixing zone width grows approximately proportional to $\sim t^{1/7}$, whereas the integral length scale in the homogeneous directions grows as $\sim t^{2/7}$. Various growth rate exponents Θ have been proposed in the past ranging from $\Theta = 2/7$ [37] to $\Theta = 2/3$ [38]. Our results are in the lower range of previously published data.

A summary of all length scales is given in Fig. 8. It shows the mixing zone width, the integral length scale, the Taylor microscale, and the Kolmogorov length scale for the three investigated shock Mach numbers Ma = 1.05, Ma = 1.2, and Ma = 1.5. Figure 8 verifies the increasing separation of scales with increasing shock Mach number. Weber *et al.* [39] also presented the mixing zone width, the Taylor microscale, and the Kolmogorov length scale obtained from experimental measurements at Ma = 1.6 and Ma = 2.2. In the investigation of Weber *et al.* [39] the separation of scales appears not to depend on the shock Mach number. The Kolmogorov length scale at Ma = 1.5 in our investigation has the same order of magnitude as in the experiment of Weber *et al.* [39].

C. Decaying turbulence

There are two distinct canonical cases of decaying isotropic turbulence which result from the solution of the Kármán-Howarth equation: turbulence of Saffman type with a Birkhoff-Saffman spectrum [40,41] $E(k \to 0) \sim Lk^2$ and turbulence of Batchelor type $E(k \to 0) \sim Ik^4$, where $L = \int \langle \boldsymbol{u} \times \boldsymbol{u'}\rangle d\boldsymbol{r}$ and $I = \int \boldsymbol{r}^2 \langle \boldsymbol{u} \times \boldsymbol{u'}\rangle d\boldsymbol{r}$ are known as Saffman and Loitsyansky

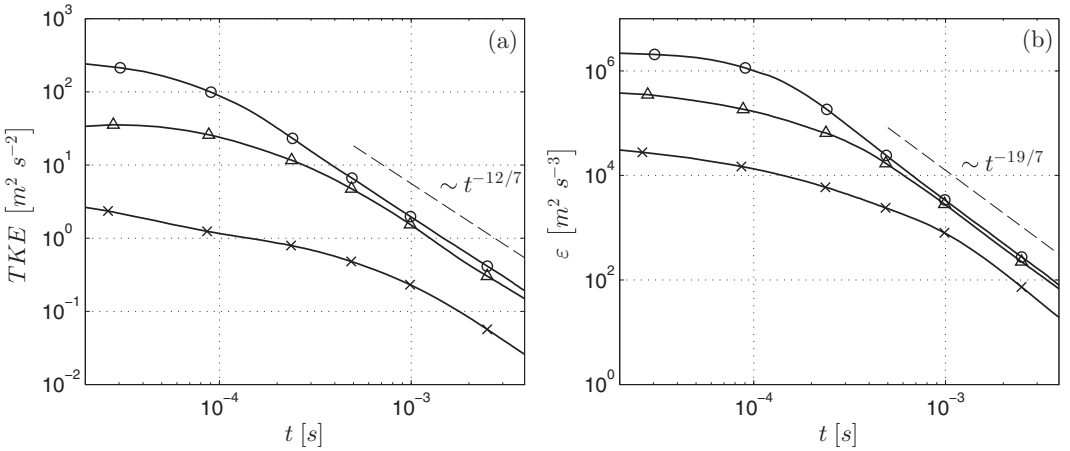

FIG. 9. Average turbulence kinetic energy TKE and viscous dissipation rate ε in the inner mixing zone as functions of time for Ma = 1.05 (crosses), Ma = 1.2 (triangles), and Ma = 1.5 (circles).

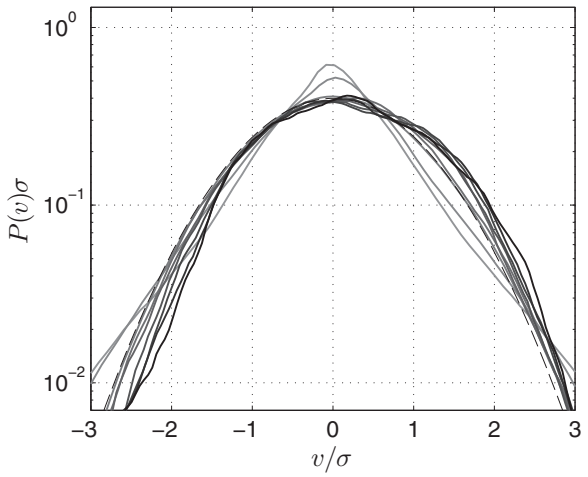

FIG. 10. Normalized probability density functions of the velocity for Ma = 1.5. The gray scale changes from light gray to black as time increases. The Gaussian distribution is given by the dashed line. The PDFs are normalized by their standard deviation σ.

integrals, respectively. These two canonical cases have been derived under the assumption that the triple velocity correlation tensor as well as the pressure-velocity correlation decay fast enough for remote points.

The Saffman integral L is an invariant provided that the triple velocity correlation tensor and the pressure-velocity correlation decay as $O(r^{-2})$ implying that the global linear momentum is conserved. Saffman [41] showed that in this case the Saffman integral is proportional to $L \sim u^2 l^3$. Then the decay of turbulence kinetic energy follows as $u^2 \sim t^{-6/5}$, whereas the integral scale grows proportional to $l \sim t^{2/5}$.

If the long-range statistics become uncorrelated according to $O(r^{-4})$, i.e., if turbulence is dominated by angular momentum with negligible linear momentum the Loitsyansky integral I is conserved [42]. Given that $I = \text{const}$ and that the large scales evolve in a self-similar way, the Loitsyansky integral is proportional to $I \sim u^2 l^5$ [32] implying that the turbulence kinetic energy of isotropic homogeneous turbulence decays as $u^2 \sim t^{-10/7}$, whereas the integral scale grows as $l \sim t^{2/7}$.

Ishida *et al.* [43] reported the kinetic energy of isotropic turbulence to decay as $\sim t^{-n}$ with $n \approx 1.4$, if the Loitsyansky integral is constant and if the Taylor microscale Reynolds number exceeds $\mathrm{Re}_\lambda > 100$. Long-range interactions between remote eddies resulted in a deviation from $I = \text{const}$ and thus in $n \neq 10/7$.

In Fig. 9 the average turbulence kinetic energy in the inner mixing zone is shown for shock Mach numbers Ma = 1.05, Ma = 1.2, and Ma = 1.5. After an initial transient all cases exhibit a decay exponent close to $n = 12/7 \approx 1.71$, which is steeper than predicted by the third hypothesis of Kolmogorov [32], i.e., $n = 10/7$. Ishida *et al.* [43], however, found that $n \to 1.5$ for $\mathrm{Re}_\lambda = 62.5$ and for lower Reynolds numbers ($\mathrm{Re}_\lambda = 31.3$) $n \to 1.63$, while $n \to 10/7$ for $\mathrm{Re}_\lambda = 125$ from which the authors concluded that the Reynolds number must exceed $\mathrm{Re}_\lambda \approx 100$ in order to observe $n = 10/7$. In the present simulations the Taylor microscale Reynolds numbers are $\mathrm{Re}_\lambda \sim O(10)$ for the two higher shock Mach number and $\mathrm{Re}_\lambda \lesssim O(10)$ for Ma = 1.05 at late times as depicted in Fig. 5. For the highest shock Mach number Ma = 1.5 the Taylor microscale Reynolds number is $\mathrm{Re}_\lambda \approx 140$ after shock passage and decays to $\mathrm{Re}_\lambda \approx 20$ at the latest time. Burattini *et al.* [44] found a dependency between the initial Reynolds number $\mathrm{Re}_\lambda(t = 0)$ and the observed decay exponent n of turbulence kinetic energy, that is, $n \to 1$ as $\mathrm{Re}_\lambda(t = 0) \to \infty$. This dependence approximately follows $n = 1.05 + 60/\mathrm{Re}_\lambda(t = 0)$ in good agreement with other data from the literature. For an initial Taylor microscale Reynolds number of $\mathrm{Re}_\lambda(t = 0) \approx 140$ the power-law exponent becomes $n \approx 1.48$ and thus is smaller than the observed value in the present investigation. Samtaney *et al.* [45] investigated decaying compressible turbulence and found for a range of different initial conditions the decay exponent of turbulence kinetic energy to be in the range $1.37 \leqslant n \leqslant 1.71$, which is in good agreement with the present results.

It is interesting to note that all three cases follow the same decay law and do not show a dependence on the initial Reynolds number as observed previously [43,44]. Also, the lowest Mach number case follows $\sim t^{-12/7}$ even though the flow does not become turbulent. Lombardini *et al.* [9] investigated shock-initiated decaying turbulence at various shock Mach numbers ranging from Ma = 1.05 to Ma = 5.

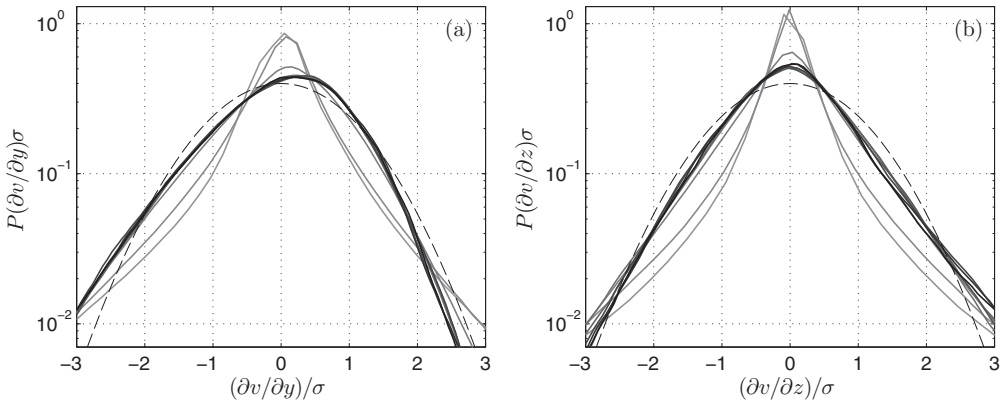

FIG. 11. Normalized probability density function of the longitudinal (a) and transverse velocity gradients (b) for Ma = 1.5. The gray scale changes from light gray to black as time increases. The Gaussian distribution is given by the dashed line. The PDFs are normalized by their standard deviation σ.

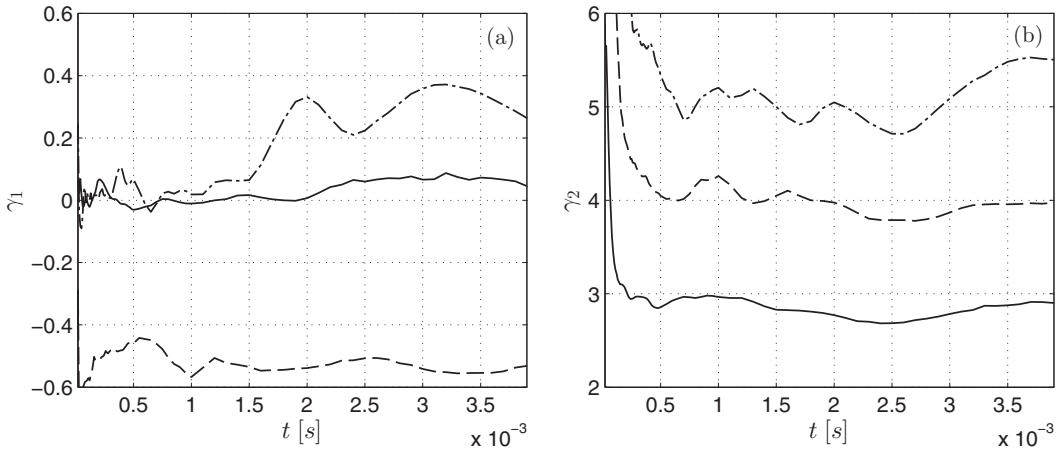

FIG. 12. Skewness (a) and kurtosis (b) of the velocity (solid line), the longitudinal velocity gradient (dashed line), and the transverse velocity gradient (dashed-dotted) for Ma = 1.5.

The turbulence kinetic energy decay was found to be larger than $\sim t^{-6/5}$ and closer to $\sim t^{-10/7}$, independent of the shock Mach number. Tritschler *et al.* [15] also found the decay of turbulence kinetic energy to be proportional to $\sim t^{-10/7}$.

Figure 9(b) shows the average viscous dissipation rate in the inner mixing zone as a function of time. The viscous dissipation rate decays as $\sim t^{-19/7}$, consistent with the decay of turbulence kinetic energy.

D. Probability density functions

According to the theory of Kolmogorov, the probability density function (PDF) of the velocity field of homogeneous isotropic turbulence exhibits a Gaussian normal distribution. However, Batchelor [46] showed that velocity gradients, especially for scales that are close to the dissipation limit, do not satisfy the assumption of uncorrelated long-range interactions.

Jiménez *et al.* [47] investigated the vorticity statistics of forced isotropic turbulence at Taylor microscale Reynolds numbers ranging from $\mathrm{Re}_\lambda = 35$ to $\mathrm{Re}_\lambda = 170$. This work indicates that the PDF of the single-point vorticity and the PDF of strain of isotropic turbulence is non-Gaussian and shows growing tails with increasing Reynolds numbers. Furthermore, the tails of the PDF do not show an asymptotic behavior for the limiting case $\mathrm{Re} \to \infty$. Despite the deviations from Gaussianity and the lack of an asymptotic behavior, the spectra showed a $k^{-5/3}$ decay law and a dissipation range as predicted by Kolmogorov. Jiménez *et al.* [47] explained this observation with long coherent vortices ("worms"). The authors state that these worms are part of the background vorticity and responsible for a large amount of turbulent dissipation. The worms themselves, however, are only responsible for a small fraction of kinetic energy which is proportional to the volume fraction that they occupy.

Wilczek *et al.* [48] found that decaying and forced turbulence do not differ fundamentally, since the velocity component PDFs show self-similarity when normalized by the respective standard deviation. Furthermore, the vorticity distribution exhibits an intermittent behavior as reported by Jiménez *et al.* [47]. The velocity distribution deviates from a Gaussian distribution with sub-Gaussian tails, implying a kurtosis of $\gamma_2 < 3$.

We show the statistics of the velocity and the transverse and longitudinal velocity gradients of the Ma = 1.5 case in Fig. 10 and Fig. 11. At lower Mach numbers the PDF show qualitatively a similar behavior as the PDFs for a shock Mach number of Ma = 1.5.

The PDFs are normalized by their respective standard deviation σ. At later times the PDFs collapse, indicating a self-similar decay as proposed previously [48]; see Fig. 10. The PDFs of velocity are approximately Gaussian, with a kurtosis slightly below that of the Gaussian distribution, i.e., $\gamma_2 \approx 2.8$. This is in very good agreement with previous results [47] for sustained isotropic turbulence, which found $\gamma_2 = 2.8$ for $\mathrm{Re}_\lambda = 35.1$. The skewness is expected to be zero in isotropic turbulence. In the present case, it fluctuates around zero before finally deviating to $\gamma_1 > 0$ and approaching $\gamma_1 \approx 0.05$ at later times; see Fig. 12(a) and Fig. 12(b).

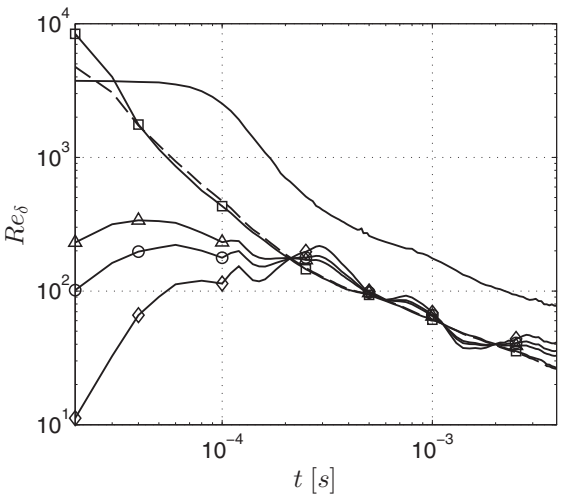

FIG. 13. Temporal evolution of different Reynolds number approximations for a shock Mach number of Ma = 1.5 [36] and as given in Table II.

TABLE II. Reynolds number approximations for a shock Mach number of Ma = 1.5 [36].

Re_δ	$\frac{\delta_x \dot{\delta_x}}{\nu}$	$\left(\frac{\Lambda}{\eta}\right)^{4/3}$	$\frac{\mathrm{TKE}^{1/2}\Lambda}{\nu}$	$\left(\frac{\sqrt{10}\Lambda}{\lambda_T}\right)^2$	$\frac{1}{100}\left(\frac{\lambda_T}{\eta}\right)^4$	$\frac{3}{20}\mathrm{Re}_\lambda^2$
$\mathrm{Re}_\delta(t = 200\ \mu\mathrm{s})$	701	171	176	165	183	188
Symbol	Solid	Circle	Triangle	Diamond	Square	Dashed

The PDFs of the velocity gradients are clearly non-Gaussian with long tails. The values of the statistical moments γ_1, γ_2 are in very good agreement with that observed previously [47]. For the longitudinal velocity gradient $\partial v/\partial y$, shown in Fig. 11(a), we find the skewness and kurtosis [see Fig. 12(a) and Fig. 12(b)] to be only slightly smaller than that given by Ref. [47] at $\mathrm{Re}_\lambda = 35.1$ ($\gamma_1 = -0.49$, $\gamma_2 = 4.2$) and Ref. [45] ($-0.5 \leqslant \gamma_1 \leqslant -0.4$) and in very good overall agreement. Note that the Taylor microscale Reynolds number is $\mathrm{Re}_\lambda \approx 15$–$25$ at later times, which is smaller than the lowest Reynolds number investigated in Ref. [47] of $\mathrm{Re}_\lambda = 35.1$.

The transverse velocity gradient $\partial v/\partial z$ shows good agreement with that of Ref. [47], but begins to deviate at later times becoming more skewed. The kurtosis γ_2 of the transverse velocity gradient agrees well with the value in Ref. [47], which found $\gamma_2 = 5.7$ for $\mathrm{Re}_\lambda = 35.1$.

Inspecting the compensated spectra of turbulence kinetic energy, shown in Fig. 6, it is evident that for times $t > 1000\ \mu$s, the spectrum is very shallow with a large portion within the dissipation range. The present data suggest that RMI exhibits features of isotropic turbulence, provided that the energy injected by the shock wave is strong enough to create a range of uncoupled scales, which is the case in the present investigation for $\mathrm{Re}_\lambda \gtrsim 35$–$80$.

E. Outer-scale Reynolds number

For Richtmyer-Meshkov unstable flows the outer-scale Reynolds number is estimated from the mixing zone width δ_x and its growth rate $\dot{\delta_x}$ according to

$$\mathrm{Re}_\delta = \frac{\delta_x \dot{\delta_x}}{\nu}. \tag{31}$$

The temporal evolution of Re_δ as given in Eq. (31) together with length scale approximations for isotropic turbulence as given in Ref. [36] are shown in Fig. 13 and listed in Table II. As also reported in Ref. [39] the approximation given in Eq. (31) overestimates the true Reynolds number in RMI, see Table II. $\mathrm{Re}_\delta = 3/20\mathrm{Re}_\lambda^2$ can be considered as reference since it is derived from the exact definition of the Taylor microscale Reynolds number. According to the outer-scale Reynolds number approximations given in Table II the Reynolds number is in the range $165 \lesssim \mathrm{Re}_\delta \lesssim 188$ at $t = 200\ \mu$s.

VI. CONCLUSION

Because direct numerical simulations (DNSs) of experimental-scale setups are beyond todays computational resources, DNSs on a reduced computational domain were performed. For this reduced computational domain we have presented fully resolved DNS results for the Richtmyer-Meshkov instability evolving from a deterministic multimode planar interface. The interface was accelerated by three different shock waves of strength Ma = 1.05, Ma = 1.2, and Ma = 1.5.

While at the lowest Mach number the dominant modes slowly mix with the ambient fluid by viscous diffusion, a turbulent mixing zone is obtained at the highest shock Mach number. An uncoupled range of scales evolves associated with the emergence of a narrow Kolmogorov inertial subrange for $t \lesssim 200\ \mu$s at Ma = 1.5. The Taylor microscale Reynolds number decreases after the shock passage from $\mathrm{Re}_\lambda \approx 143$ to $\mathrm{Re}_\lambda \approx 13$ at the final time. Increasing the shock Mach number leads to larger Taylor microscale Reynolds numbers, and the scales of turbulent motion become more and more separated.

The growth of integral scale and mixing zone width as well as the decay rates of turbulence kinetic energy and enstrophy are independent of the shock Mach number and in good agreement with values known from decaying isotropic turbulence.

Probability density functions of the velocity and its longitudinal and transverse derivatives are also in agreement with those for decaying isotropic turbulence.

We conclude that turbulence evolving from the Richtmyer-Meshkov instability is not fundamentally different from decaying isotropic turbulence despite being only isotropic and homogeneous in two spatial directions. This is particularly true when the Reynolds number exceeds a critical value and the flow becomes turbulent. The critical Taylor microscale Reynolds number was found to be $\mathrm{Re}_\lambda \gtrsim 35$–$80$ for the investigated relatively low shock Mach numbers.

ACKNOWLEDGMENTS

V.K.T. thanks S. K. Lele and B. J. Olson for many fruitful discussions and for valuable insights. We want to acknowledge the Gauss Centre for Supercomputing e.V. for providing computing time on the GCS Supercomputer SuperMUC at Leibniz Supercomputing Centre.

[1] G. Taylor, Proc. R. Soc. Lond. A **201**, 192 (1950).
[2] R. D. Richtmyer, Comm. Pure Appl. Math. **13**, 297 (1960).
[3] E. E. Meshkov, Fluid Dyn. **4**, 101 (1969).
[4] M. Brouillette, Annu. Rev. Fluid Mech. **34**, 445 (2002).
[5] J. G. Wouchuk and K. Nishihara, Phys. Plasmas **4**, 1028 (1997).
[6] J. G. Wouchuk, Phys. Rev. E, **63**, 056303 (2001).
[7] N. J. Zabusky, Annu. Rev. Fluid Mech., **31**, 495 (1999).
[8] D. J. Hill, C. Pantano, and D. I. Pullin, J. Fluid Mech. **557**, 29 (2006).
[9] M. Lombardini, D. I. Pullin, and D. I. Meiron, J. Fluid Mech. **690**, 203 (2012).
[10] F. F. Grinstein, A. A. Gowardhan, and A. J. Wachtor, Phys. Fluids **23**, 034106 (2011).
[11] O. Schilling and M. Latini, Acta Math. Scientia **30**, 595 (2010).

[12] B. Thornber, D. Drikakis, D. L. Youngs, and R. J. R. Williams, Phys. Fluids **23**, 095107 (2011).
[13] J.-S. Bai, J.-H. Liu, T. Wang, L.-Y. Zou, P. Li, and D.-W. Tan, Phys. Rev. E **81**, 056302 (2010).
[14] J.-S. Bai, B. Wang, T. Wang, and K. Liu, Phys. Rev. E **86**, 066319 (2012).
[15] V. K. Tritschler, B. J. Olson, S. K. Lele, S. Hickel, X. Y. Hu, and N. A. Adams, J. Fluid Mech. **755**, 429 (2014).
[16] C. Weber, N. Haehn, J. Oakley, D. Rothamer, and R. Bonazza, Phys. Fluids **24**, 074105 (2012).
[17] V. K. Tritschler, S. Hickel, X. Y. Hu, and N. A. Adams, Phys. Fluids **25**, 071701 (2013).
[18] A. W. Cook, Phys. Fluids **21**, 055109 (2009).
[19] B. E. Poling, J. M. Prausnitz, and J. P. O'Connell, *The Properties of Gases and Liquids* (McGraw-Hill, New York, 2001).
[20] P. D. Neufeld, A. R. Janzen, and R. A. Aziz, J. Chem. Phys. **57**, 1100 (1972).
[21] X. Y. Hu, Q. Wang, and N. A. Adams, J. Comp. Phys. **229**, 8952 (2010).
[22] X. Y. Hu and N. A. Adams, J. Comp. Phys. **230**, 7240 (2011).
[23] X. Y. Hu, V. K. Tritschler, S. Pirozzoli, and N. A. Adams, arXiv:1204.5088.
[24] P. L. Roe, J. Comp. Phys. **43**, 357 (1981).
[25] B. Larouturou and L. Fezoui, in *Nonlinear Hyperbolic Problems*, Lecture Notes in Mathematics vol. 1402 (Springer, Berlin, 1989), p. 69.
[26] E. F. Toro, *Riemann Solvers and Numerical Methods for Fluid Dynamics* (Springer, Berlin, 1999).
[27] S. Gottlieb and C.-W. Shu, Math. Comp. **67**, 73 (1998).
[28] V. K. Tritschler, X. Y. Hu, S. Hickel, and N. A. Adams, Phys. Scr. T **155**, 014016 (2013).
[29] V. K. Tritschler, A. Avdonin, S. Hickel, X. Y. Hu, and N. A. Adams, Phys. Fluids **26**, 026101 (2014).
[30] P. Yeung and S. Pope, J. Fluid Mech. **207**, 531 (1989).
[31] P. E. Dimotakis, J. Fluid Mech. **409**, 69 (2000).
[32] A. N. Kolmogorov, Dokl. Akad. Nauk SSSR **31**, 538 (1941).
[33] S. G. Saddoughi and S. V. Veeravalli, J. Fluid Mech. **268**, 333 (1994).
[34] Y. Zhou, H. F. Robey, and A. C. Buckingham, Phys. Rev. E **67**, 056305 (2003).
[35] H. Robey, Y. Zhou, A. Buckingham, P. Keiter, B. Remington, and R. Drake, Phys. Plasmas **10**, 614 (2003).
[36] S. B. Pope, *Turbulent Flows* (Cambridge University Press, Cambridge, 2000).
[37] A. Llor, European J. Mech. B **30**, 480 (2011).
[38] D. L. Youngs, Laser Part. Beams **12**, 725 (1994).
[39] C. R. Weber, N. S. Haehn, J. G. Oakley, D. A. Rothamer, and R. Bonazza, J. Fluid Mech. **748**, 457 (2014).
[40] G. Birkhoff, Comm. Pure Appl. Math. **7**, 19 (1954).
[41] P. G. Saffman, J. Fluid Mech. **27**, 581 (1967).
[42] L. G. Loitsyansky, Trudy Tsentr. Aero.-Giedrodin Inst. **440**, 3 (1939).
[43] T. Ishida, P. A. Davidson, and Y. Kaneda, J. Fluid Mech. **564**, 455 (2006).
[44] P. Burattini, P. Lavoie, A. Agrawal, L. Djenidi, and R. A. Antonia, Phys. Rev. E **73**, 066304 (2006).
[45] R. Samtaney, D. I. Pullin, and B. Kosovic, Phys. Fluids **13**, 1415 (2001).
[46] G. K. Batchelor, *The Theory of Homogeneous Turbulence* (Cambridge University Press, Cambridge, 1953).
[47] J. Jiménez, A. A. Wray, P. G. Saffman, and R. S. Rogallo, J. Fluid Mech. **255**, 65 (1993).
[48] M. Wilczek, A. Daitche, and R. Friedrich, J. Fluid Mech. **676**, 191 (2011).